이학박사 학위논문

Automated Assessment of Genotoxicity Using Mutant Drosophila Hair Images

(돌연변이 초파리 털 영상을 이용한 유전독성의 자동화된 평가)

2015년 2월

서울대학교 대학원

협동과정 계산과학전공

곽 지 훈

Automated Assessment of Genotoxicity Using Mutant Drosophila Hair Images

(돌연변이 초파리 털 영상을 이용한
유전독성의 자동화된 평가)

지도교수 강 명 주

이 논문을 이학박사 학위논문으로 제출함

2014 년 12 월

서울대학교 대학원

협동과정 계산과학전공

곽 지 훈

곽지훈의 이학박사 학위논문을 인준함

2014 년 12 월

위 원 장 _____ (인)
부위원장 _____ (인)
위 원 _____ (인)
위 원 _____ (인)
위 원 _____ (인)

Ph.D. Dissertation

Automated Assessment of Genotoxicity Using Mutant Drosophila Hair Images

(돌연변이 초파리 털 영상을 이용한 유전독성의 자동화된 평가)

by

Jihoon Kwak

February 2015

Interdisciplinary Program in
Computational Science and Technology
Seoul National University

Abstract

In this work, the SMART assay, a genotoxicity test using mutant Drosophila hairs, was automated. The SMART assay assesses the genotoxicity of a chemical compound by counting mutant hairs on the Drosophila's wings. Even though the Drosophila has many advantages in cost and ethnic problems, the speed and accuracy are limited, since the counting is manual. So far, no research has been given to the automation of SMART assay. For the first time, an automated image analysis system that counts the mutant hairs automatically was developed in this work. The automation consists of four parts: image acquisition, image preprocessing, hair detection, and mutant classification. In each part, new automation methods are proposed. In the image acquisition, a wing detection method using ellipse detection and an optimizing method for image acquisition using the wing detection are proposed. In the image preprocessing, the hair image separation into upper and lower using a wind surface reconstruction is proposed, and the hair area segmentation is proposed. In hair detection, a line fitting method in 3D is proposed. In mutant classification, a upper and lower classification and mutant classification using the wing surface are proposed. The proposed system is validated using the proposed automatic matching system. The genotoxicity of the automated SMART assay coincides with that of the original manual SMART assay.

Keywords: Hair Detection, Automated Assessment, Genotoxicity Test, SMART Assay, Drosophila, Mutant Phenotype

Student Number: 2004-20631

Contents

List of Figures

List of Tables

List of Algorithms

Chapter 1

Introduction

The genotoxicity is one of the most serious side effects of toxic drugs. It damages the genetic information within a cell causing mutations, which may lead to cancer. In the drug discovery Fig. 1.1, after a chemical compound was proved that it cures a disease, it's safety should be tested. Before testing on human, animals such as mouse, dog, monkey and pig are tested on. But, the such mammals have the ethnic, cost and time problems. The Bacterial Reverse Mutation Assay, also known as the Ames Assay use bacteria [1]. But the genetic similarity between human and bacteria is much less than that between human and mammals. Insects has the genetic similarity between them. They are chip and have no ethnic issue. Moreover the life cycle is much shorter than mammals.

The Somatic Mutation And Recombination Test (SMART) using drosophila is well known genotoxicity assessment method[2]. Drosophila, also known as fruit fly, has some mutant phenotypes Fig. 2.1. If mutant and normal flies are crossed, no mutant phenotype appears in natural case. But, if the larva eats toxic compound, mutant phenotype appears. The mutant frequency shows the genotoxicity. However, due to

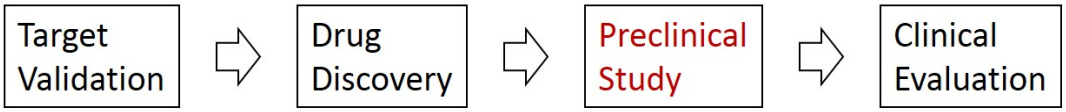

Figure 1.1 Drug discovery process. The preclinical study tests the genotoxicity or side effects of drugs using animals before the clinical evaluation which tests on human.

its quantitative and throughput limitation, its usage was mostly restricted in academic field. Now, the frequency is counted manually by human using the microscope. To overcome this problem, we developed the automatic readout system for SMART using the image analysis technique. This could help drug development process through providing intermediate test system which is located in between unit cell method AMES test and expensive, difficult and time-consuming animal model test. To test the genotoxicity of drugs, mutant hairs of drosophila are counted by eyes now.

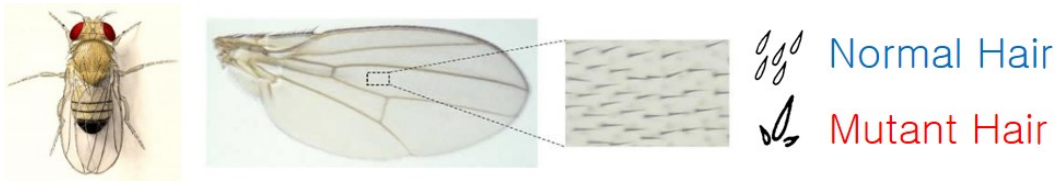

Figure 1.2 Drosophila phenotypes. Drosophila, also known as fruit fly, has three phenotypes: normal hairs, multiple wing hairs (MWH) and flair hairs. Normal hairs and multiple wing hairs are straight, while flair hairs looks like noise spots. Since the flair type are not easy to differentiate from real noise, it is not used in this work.

The Drosophila's wing (Fig. 1.4 (a)) has tiny hairs. Normal hairs (Fig. 1.4 (b)) are regularly spaced and their orientations are uniform. But, mutant hairs (Fig. 1.4 (c)) are less regularly spaced and less uniform in their orientation. Usually, two or three

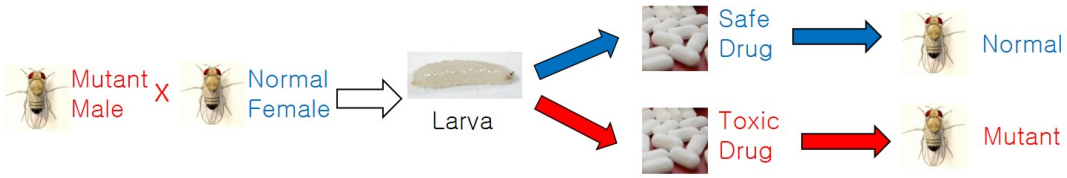

Figure 1.3 SMART assay process. If the MWH male is mated with the normal female, all children are normal. But, the larva eats toxic chemical compound, it mutates and has the MWH phenotype. By counting the mutant hairs, we can test the genotoxicity of the chemical compound.

hairs are closer than others. We want to count such mutant hairs automatically. In the beginning of this work, we faced some challenging problems Fig. 1.5. The first problem is out-of-focus Fig. 1.5(1). Since the wing surface is not flat, it is hard to take a clean image focused in all the hairs. The Second problem is the overlap of upper and lower hairs Fig. 1.5(b). Flies have hairs on both side of wings. If they are overlapped in a image, it is hard to distinguish the mutant hairs from the normal hairs from the opposit side. The third is how to detect each hairs Fig. 1.5(c). The hairs on one side are also overlapped. Since the tips of some hairs touch the root of other hairs, it looks like a long one hair. The last is how to classify mutant hairs among the detected hairs Fig. 1.5(d). There are critical artifacts on image. The roots of hairs from the other side appear as small dots, which might be confused mutant hairs.

In this work, I resolved the above problems and proposed the automated mutant hair counting system in Drosophila wing images. I developed an image acquisition method using multi-focused image stack, some image preprocessing methods, an hair detection method using a new line fitting method, and a mutant classification method. Fig. 1.6 is the overview of the automated SMART assay, and Alg. 1 is the corresponding process. It consists of five phases. The details will be explained in following

chapters.

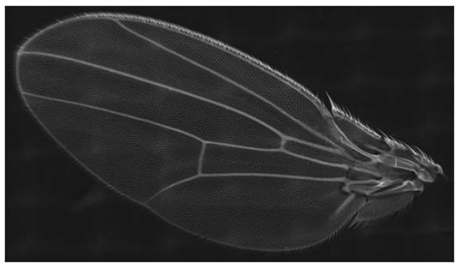

(a) Drosophila's Wing

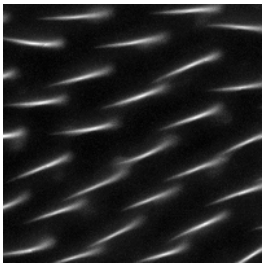

(b) Normal hairs

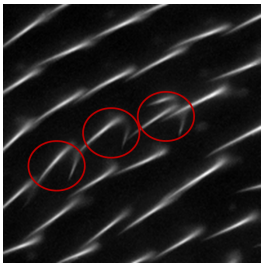

(c) Mutant hairs

Figure 1.4 Hairs on a Drosophila's wing. (a) An image of a Drosophila's wing. (b) Normal hairs of Drosophila are regularly spaced, and the orientations are also uniform. (c) Mutant hairs are less regularly spaced and less uniform in orientation.

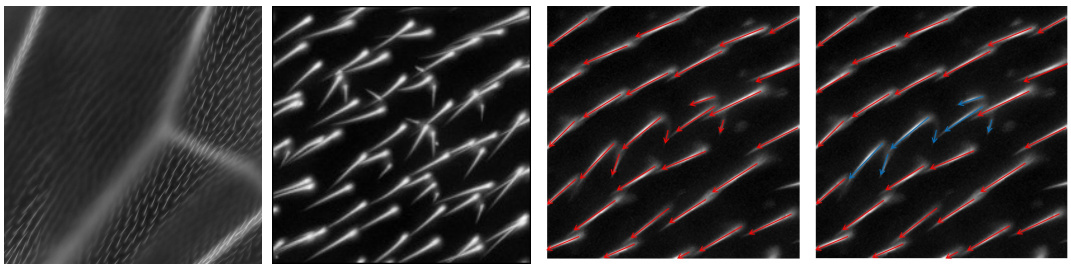

(a) Out of focus (b) Overlap (c) Detection (d) Classification

Figure 1.5 Challenging problems. (a) Since the wing surface is not flat, some parts of the image are out of focus, while some parts are in focus. (b) The wing has hairs on both side. So, the upper hairs and lower hairs are overlapped in the projection image. (c) The detection of hair has some difficulties, e.g. noise from hair roots, overlapping with same side hairs, slightly bending hairs. (d) The mutant classification also has some difficulties, most of those are due to wrong hair detections.

Algorithm 1 The whole process of automated SMART assay

Phase 1: Wing Slide Preparation

1: Drug: Given drugs, make different concentrations.

2: Fly Culturing: Culture flies and feed them the drug.

3: Wing Slide: Make slide glasses of wings.

Phase 2: Image Acquisition

4: Wing Scan: Scan the wing slides.

5: Wing Detection: Detect two end points of wings.

6: Image Position: Calculate x-y positions to be taken images.

7: Wing Imaging: Take digital images of wing slide.

Phase 3: Image Preprocessing

8: Wing Surface Reconstruction: Reconstruct the surface between the upper and lower hairs.

9: Projection Images: Calculate the projections of image stack.

10: Hair Area Segmentation: Segment hair area from wing images.

Phase 4: Hair Detection

11: Location: Calculate the initial guess of the locations of hairs.

12: Direction: Calculate the initial guess of the directions of hairs.

13: Length: Calculate the initial guess of the lengths of hairs.

14: Line Fitting: Fit the initial directional line segments to the hairs.

Phase 5: Classification

15: Upper and Lower: Classify hairs into upper and lower hairs.

16: Normal and Mutant: Classify hairs into normal and mutant hairs.

17: Genotoxicity: Determine the genotoxicity of the drugs.

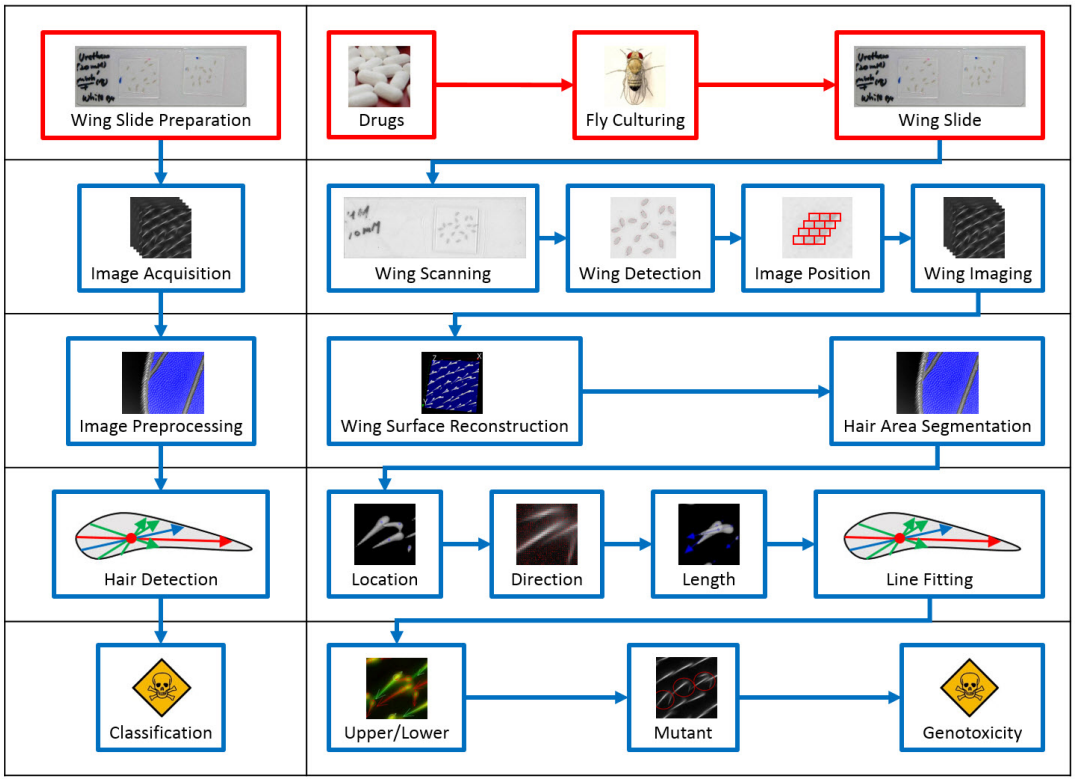

Figure 1.6 Overview of automated assessment. This is the whole process of the automated SMART assay. The red parts are manual and the blue part are all automated. The red parts are same as the original SMART assay except the phenotype simplification, and the manual mutant hair counting step in the original SMART assay is replaced by the blue parts.

Chapter 2

Wing Slide Preparation

In this chapter, the process of wing slide preparation will be briefly explained. It is a biological part of automated SMART assay. The work in this chapter is done by Dr. Chun Taek Oh in Drug Biology Group of Institut Pasteur Korea. The process includes the some choices: chemical compounds, mutant phenotypes, and culturing conditions. They are chosen to validate the automated SMART assay efficiently and effectively. The wing slide preparation is the only manual part in the automated SMART assay. There are some processes that could be possibly automated, for example, automated wing cutting. However, nothing seems suitable for automation by image analysis. The protocol of the preparation in automated SMART assay is just same as that of the original SMART assay. After the wing slide is ready, human counts the hairs in the original SMART, while machine counts the hairs in automated SMART.

2.1 Compounds

To validate a new toxicity test method, two types of chemical compounds should be tested: positive control and negative control. The positive control is the compound which is known as genotoxic, and the negative control is the compound known as non-genotoxic. In this work, we chose some compounds whose genotoxicities are well known by other genotoxicity tests but not yet by SMART assay. Anipyrin, Atenolol and Isoniazid are used as negative controls, and Mitomycin C, Methyl methanesulfonate and Urethane are used as positive controls.

2.2 Phenotypes

The original SMART assay uses two phenotypes of Drosophila:multiple wing hair (mwh) phenotype and flair (flr) phenotype Fig. 2.1(c). mwh is characterized by that more than one hairs, usually two to four hairs, come from one cell, while only one hair rises from one cell in case of normal hair. Hence, the roots of the hairs of mwh are close to each other. But the shape of each hair of mwh is just same as the shape of normal hair, which looks like a needle or a thorn. On the other hand, the flr phenotype has a totally different shape from the normal and mwh hair. It looks like noisy flare which the name comes from. In 2D image of hairs, flr phenotype looks very similar to the roots of hairs from the other side of wing.

In the early state of this work, only 2D image analysis was considered. So, the flr phenotype was excluded to make the automated mutant hair counting more robust. Otherwise, there would be many false detections. The original SMART assay cross mwh and flr. It was simplified by crossing mwh and normal. By the way, in the final stage of this work, 3D image was successfully analyzed. In 3D, the root of the other side hair is no more similar to flr phenotype. So, the our automated system could be easily applied to flr phenotype.

2.3 Culturing Conditions

If the concentration of toxic compound is too high, the fly egg could not hatch. On the contrary, if the concentration is too low, there is no mutant hair even though it is known as toxic. So, the concentrations of the compound should be carefully chosen so that enough eggs hatch and the number of mutant hairs effectively show the toxicity. Figs. 2.2 and 2.3 are the chosen concentration range for each compound. For each concentration of each compound, the fly are separated in glass cylinders and cultured in a incubator Fig. 2.4. Finally, the wings are put on slide grass and covered by cover glass Fig. 2.5.

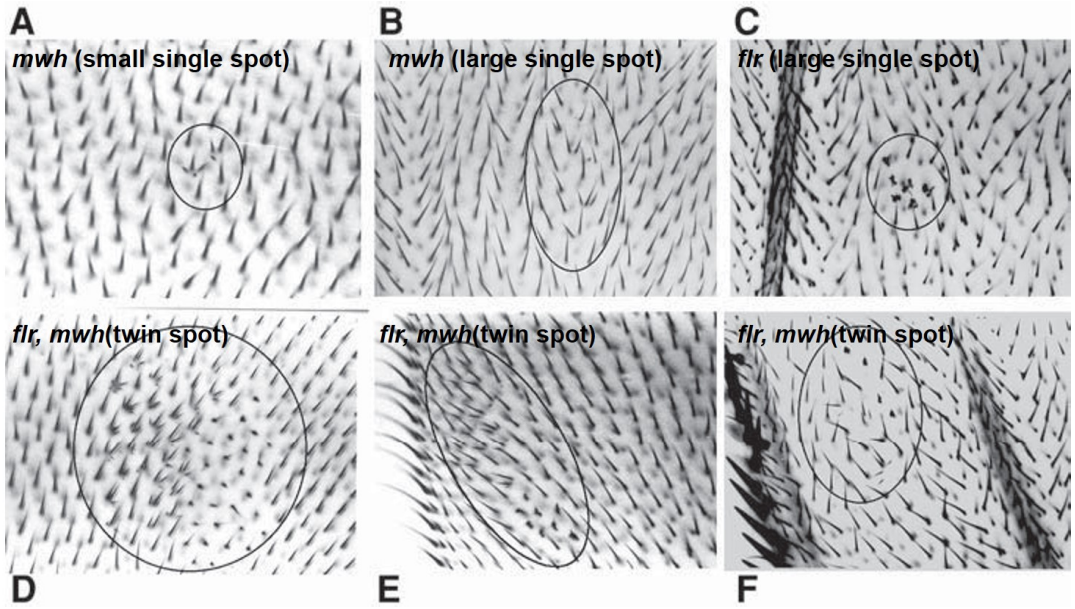

Figure 2.1 Phenotypes [8]. (a),(b) are multiple wing phenotype (mwh). (c) is flair (flr) phenotype. (d)-(f) both mwh and flr.

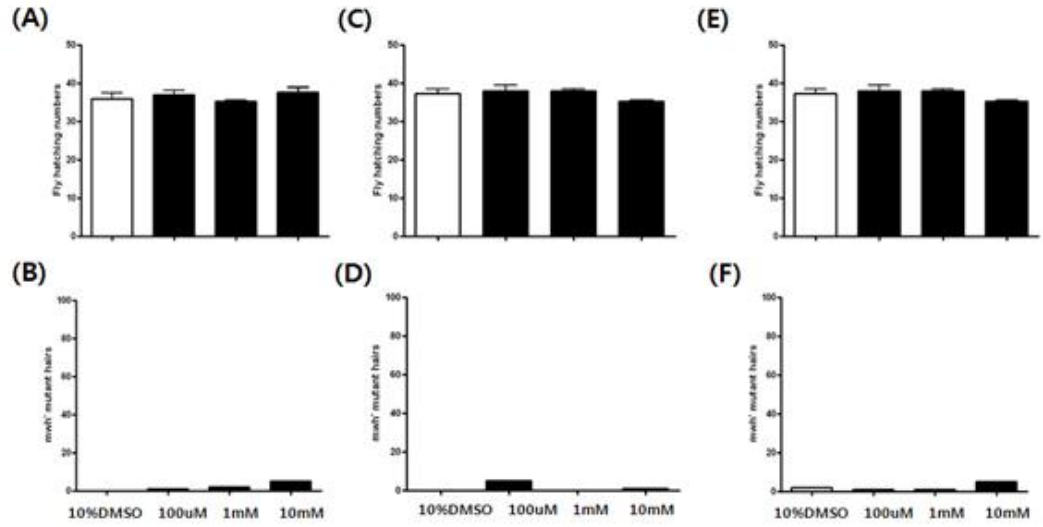

Figure 2.2 Negative Controls. The first row is fly hatching numbers for different concentrations, and the second row is mwh mutant hairs. (A), (B): Antipyrin, (C), (D): Atenolol, (E), (F): Isoniazid

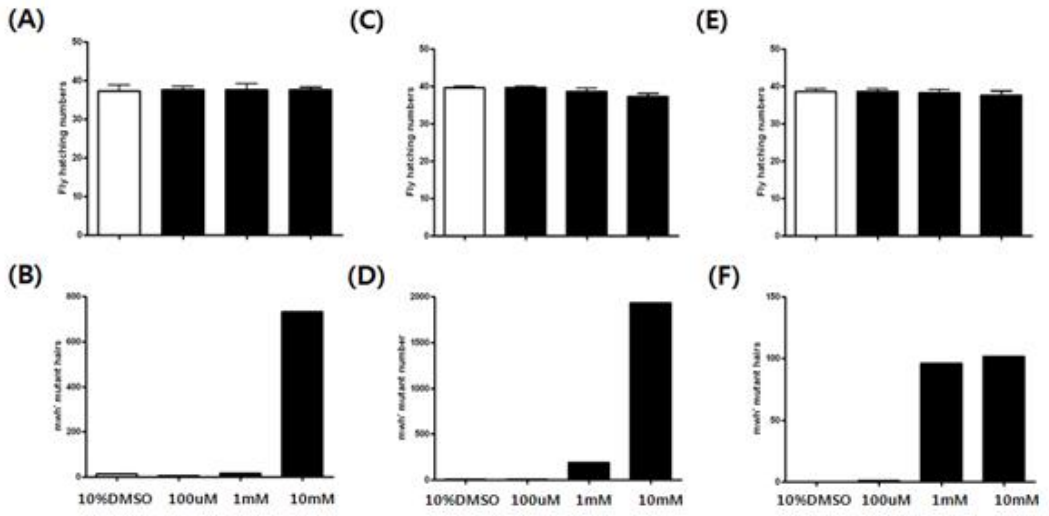

Figure 2.3 Positive Controls. The first row is fly hatching numbers for different concentrations, and the second row is mwh mutant hairs. (A), (B): Mitomycin C, (C), (D): Methyl methanesulfonate, (E), (F): Urethane

(a) Drosophila (b) Incubator (c) FlyLines (d) FlyLine

Figure 2.4 Fly Culture. (a) Drosophila is also called fruit fly (b) Flied are cultured in the incubator. (c) Different concentrations of different drugs are applied to larvae. (d) In a test tube, many flies are cultured under a same condition.

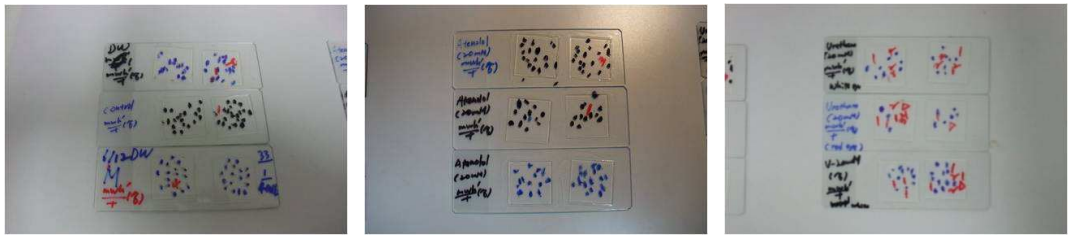

(a) Control (b) Negative Control (b) Positive Control

Figure 2.5 Wing Slides. (a) Control is flies injected only pure water. (b) Negative control is files injected ethanol, which is proved nontoxic. (c) Positive control is flies injected Urethane, which is proved toxic.

Chapter 3

Image Acquisition

3.1 Multi-focussed Image Stack

In the hair image 3.2(a), some region is out of focus, while some other region is in focus. This is because the wing surface is not flat. According to the depth of field Eq. 3.1, we can increase the depth of field to capture all the region in focus by reducing either the numerical aperture or magnification. However, if we reduce the magnification, we cannot get enough pixel resolution for image processing for any available numerical aperture. This implies that it is impossible to capture all the region in focus for image processing purpose with light microscope.

$$D = (\frac{\lambda}{N^2} + \frac{e}{NM})n, \tag{3.1}$$

where D is the depth of field, N is the numerical aperture, M is the magnification, e is the smallest resolution, λ is the wavelength, n is the refractive index [9].

So, we took multiple images 3.2(b) increasing the focus plane using the motorized stage 3.2(e). The Nikon software Fig. 3.2(d) can automatically take the vertical series

of images if we put top and bottom heights and the number of images. In the next chapter, this image stack will be used to produce one image focused over all area. It will be also used as 3D image to detect 3D hairs in it.

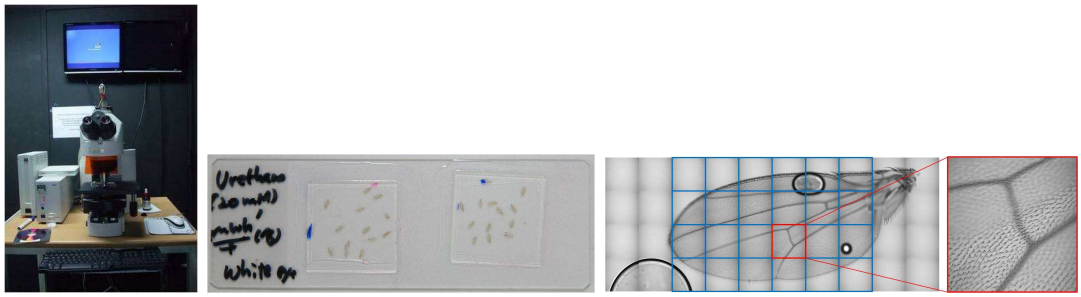

(a) Microscope (b) Slide (c) Image Patch

Figure 3.1 Image Acquisition. (a) Nikon Eclipse 90i, a light microscope is used to take images. (b) A slide have 15 to 20 wings. (c) By the Nikon imaging software, about 25 images are required to cover one wing.

3.2 Multi-position Image Slide

I proposed a automated optimal acquisition position generator. It detects wings by ellipse, and using the two end points of the ellipse, optimal positions of image acquisition are generated. With the positions, the Nikon software can take the minimum number of images which cover all wings in a slide automatically.

The Nikon software has two ways to take images at multiple positions. One is a continuous image array and the other is a list of positions. A wing slide has about 15 to 20 wings on it Fig. 3.3(a). The best automatic way to take all images that the Nikon software alone can do is taking images over all the slide area. But it is very inefficient because it takes a lot of time and memory space. If we know the position of each wing, we can take image array as Fig. 3.3(b). But half the images among the

image array have only partial or no image of hair. If we know two end points of each wing, we can reduce the number of image as Fig. 3.3(d) or (e).

[14] is a very efficient ellipse detection method when we know the boundary of object. [4] enhances the speed of [14] by dramatically reducing the calculation by randomizing. However, these method gives overlapped detection if the edge is not perfectly fitted to ellipse Fig. 3.5(d), (h). They requires the number of detection as parameter. Even though the parameter is much larger than wings, there are missing wings Fig. 3.5(c), (g).

I proposed the energy map Fig. 3.5(i), which records best wing score. We can find a unique ellipse by local maximum Fig. 3.5(j) for all wings. So, there is no overlap and no missing hair Fig. 3.5(k), (l). More over, the parameter, the number of detection is not required.

$$x_0 = (x_1 + x_2)/2 \tag{3.2}$$

$$y_0 = (y_1 + y_2)/2 \tag{3.3}$$

$$a = \sqrt{(x_2 - x_1)^2 + (y_2 - y_1)^2} \tag{3.4}$$

$$d = \sqrt{(x - x_0)^2 + (y - y_0)^2} \tag{3.5}$$

$$f = \sqrt{(x - x_2)^2 + (y - y_2)^2} \tag{3.6}$$

$$f^2 = a^2 + d^2 - 2ad\cos\tau \tag{3.7}$$

$$\frac{(x - x_0)^2}{a^2} + \frac{(y - y_0)^2}{b^2} = 1 \tag{3.8}$$

$$x - x_0 = d\cos\tau \tag{3.9}$$

$$y - y_0 = d\sin\tau \tag{3.10}$$

$$b = \sqrt{\frac{a^2 d^2 \sin^2\tau}{a^2 - d^2\cos^2\tau}} \tag{3.11}$$

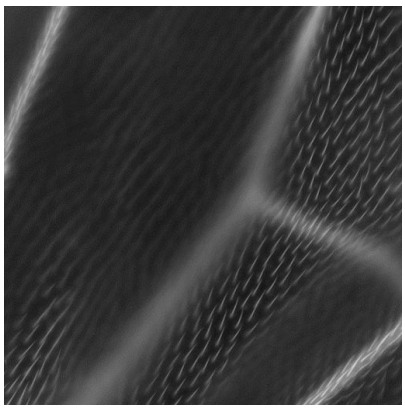

(a) Out of focus

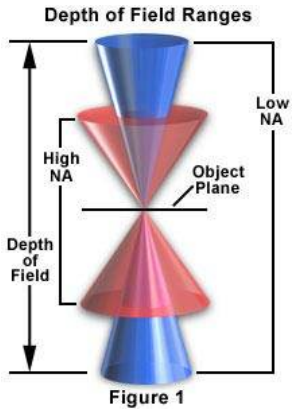

(b) Depth of field

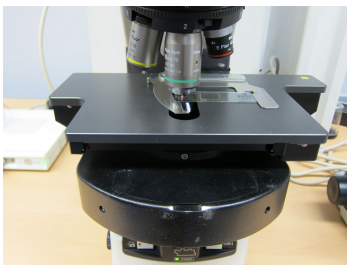

(c) Motorized stage

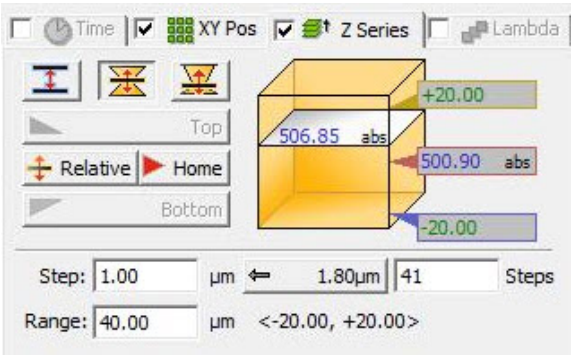

(d) Z series

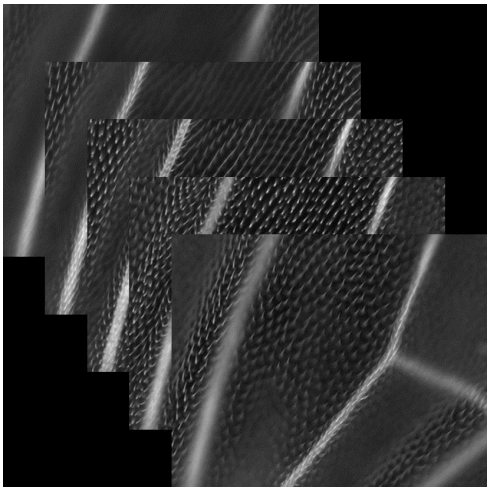

(e) Multi-focussed image stack

Figure 3.2 Multi-focussed image stack. (a) Some parts of image are out of focus. (b) The depth of field are limited since it is inversely proportional to the magnitude. (c) Motorized stage moves x, y, z directions. (d) The Nikon software can take the z-series of images automatically. (e) Multi-focussed image stack is images with different focus planes from the bottom to the top of the wing.

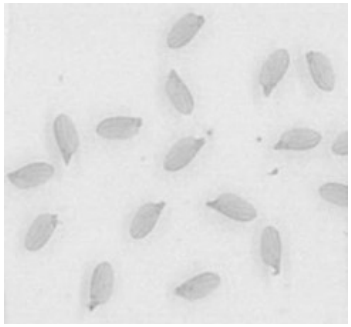

(a) Wing slide image

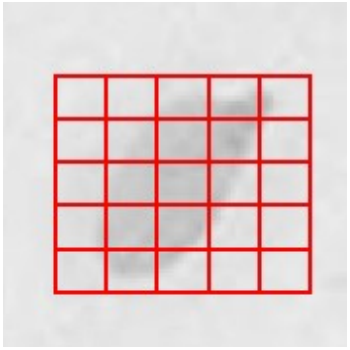

(b) 5x5 rectangular array

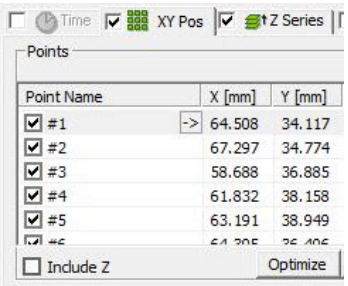

(c) XY Positions

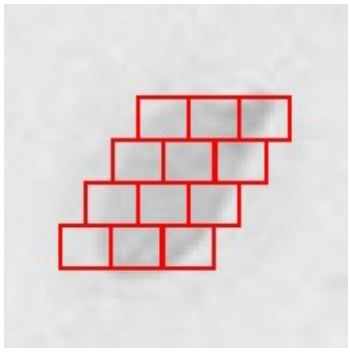

(d) 4x3 inclined array

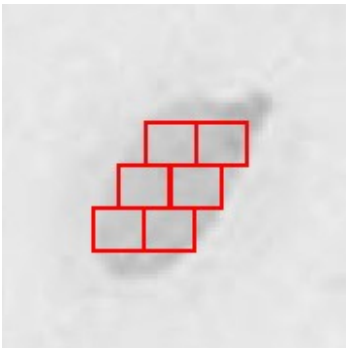

(e) 3x2 inclined array

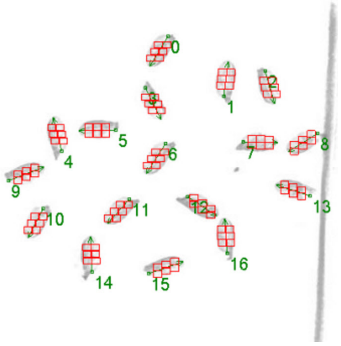

(f) Multiple image arrays

Figure 3.3 Image Array. (a) A whole slide image can be taken easily and fast by a normal document scanner. (b) At least 5x5 rectangular array is required to cover a wing. (c) If we input the list of any x-y positions, the nikon software take images automatically. (d) If the angle of a wing is given, only 3x2 inclined array can cover the whole wing. (e) 3x2 inclined array can cover more about 90% of a wing. (f) If the positions and angles of each wing are known, we can save huge amount of time and hard disk space.

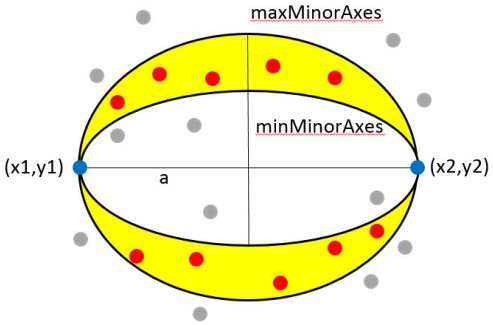

(a) The range of minor axes

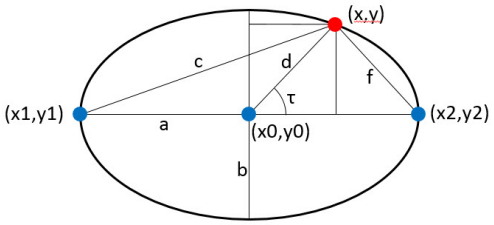

(b) Calculation of minor axes

Figure 3.4 Minor axes calculation. (a) Given the minimum and maximum of minor axes, only the points in the area between them are considered. (b) Given two end points on a ellipse's major axes, a third point determines the minor axes by the cosine rule trigonometry.

Algorithm 2 Wing Detection

For given wing slide image, $imgWing$,
$imgEdge$ = Detect edge of $imgWing$ by the Canny edge detector.
$imgSeg$ = Threshold $imgWing$ by the K-Means clustering with 2 classes.
$imgMask$ = Dilation of $imgSeg$.
$imgEdgeMasked$ = Mask $imgEdge$ with $imgMask$.
$pairsEdge$ = All pairs of two points on $imgEdgeMasked$
$pairsEdgeRandomized$ = A subset of $pairsEdge$ randomly chosen.
for each pair $\{(x1, y1), (x2, y2)\}$ in $pairsEdgeRandomized$ **do**
    if $(x0, y0)$ = the center of $\{(x1, y1), (x2, y2)\}$ is on $imgEdgeMasked$ **then**
        for each third point (x, y) in $imgEdgeMasked$ **do**
            Calculate the minor axes b when (x, y) is on the ellipse with two end points $\{(x1, y1), (x2, y2)\}$.
            if b is between the given minor axes range **then**
                Update the accumulate array of minor axes length.
            end if
        end for
        Find the maximum bin, $bMax$ of the accumulate array.
        Update the $imgEllipseEnergyMap$ at the closet pixel to $(x0, y0)$ with $bMax$
        Save the corresponding ellipse information.
        If the pixel has already a value, take the bigger value.
    end if
end for
Find local maxima of $imgEllipseEnergyMap$.
The corresponding ellipses are the wing detections.

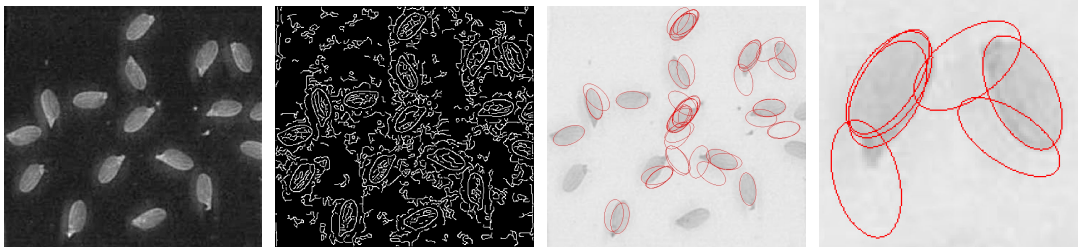

(a) Wing slide image (b) Edge (c) by [14], [4](d) Overlaps, false detections

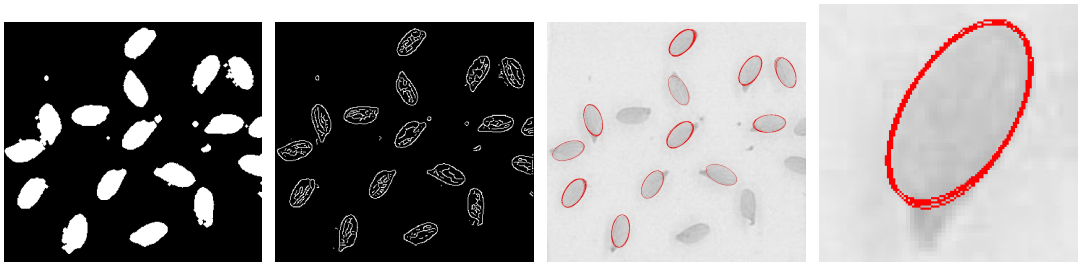

(e) Wing mask (f) Masked Edge (g) by [14], [4], mask (h) Overlaps

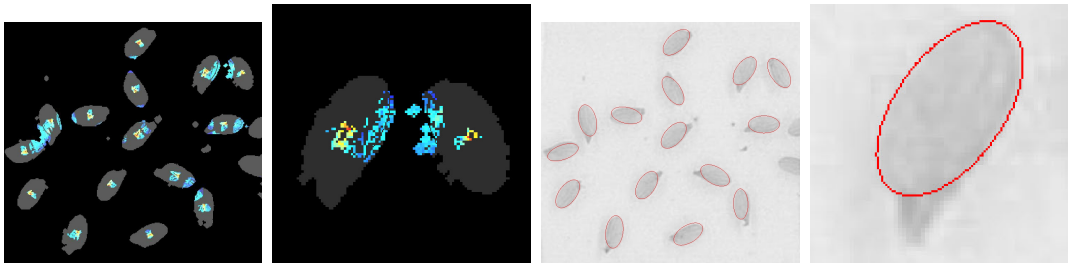

(i) Energy map (j) Local maxima (k) By energy map (l) No overlap

Figure 3.5 Ellipse detection. The ellipse detection method by [14] and [4] is fast and efficient. However, it the image has noise as (b), it gives a lot of overlapped detections and some false and missing detections. If the wing mask is used, the false detection can be reduced, but there are still missing detections. [14] need the number of ellipses to detect as a parameters. However, with a large number of detections, there are still missing detections. as in (g). (i) The proposed ellipse detection method with the energy map does not need the number of detections as a parameter, but finds all ellipses as (k), gives no overlap as (l), and is still fast.

Chapter 4

Image Preprocessing

4.1 Wing Surface Reconstruction

Applying maximum projection method to this multi-focused image stack, we get a synthetic clear image in which every hairs are focused. However, even normal hairs might be misunderstood as mutant hairs because the upper and lower hairs are overlapped in the image as Fig. 4.1 (a). So, we need to separate the upper and lower hairs. We use variation span as focusing criteria as in [11] and estimate the depth map (Fig. 4.1 (b)). Using this depth map, we can reconstruct the wing surface (Fig. 4.1 (c)), which separates the upper and lower hairs. After maximum projection on each side, we get the upper and lower hair images

$$I(i,j,k) \tag{4.1}$$

$$M(i,j) = \max_k I(i,j,k) \tag{4.2}$$

$$N_r^k(i,j) = (p,q,k) | (i-p)^2 + (j-q)^2 < r^2 \tag{4.3}$$

$$V_r^k(i,j) = \frac{\max_{(p,q)\in N_r^k(i,j)} I(i,j,k) - \min_{(p,q)\in N_r^k(i,j)} I(i,j,k)}{\sum_{(p,q)\in N_r^k(i,j)} I(i,j,k)} \tag{4.4}$$

$$D(i,j) = \arg\min_k V_k^k(i,j) \tag{4.5}$$

$$W(i,j) = GussianBlur_\delta D(i,j) \tag{4.6}$$

$$U(i,j) = \max_{k>W(i,j)} I(i,j,k) \tag{4.7}$$

$$L(i,j) = \max_{k<W(i,j)} I(i,j,k) \tag{4.8}$$

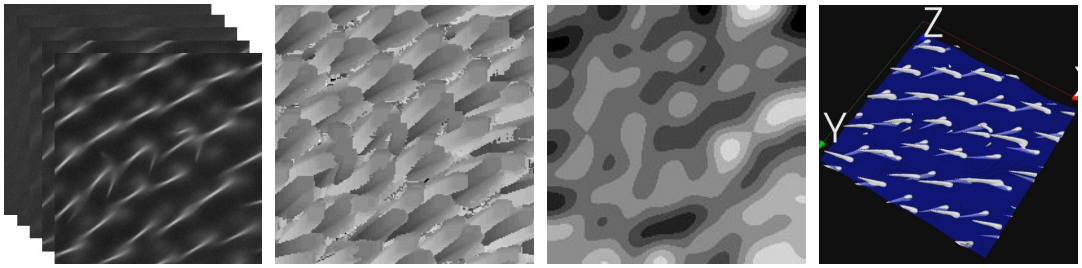

(a) Image stack (b) Depth map (c) Wing surface (d) Wing surface in 3D

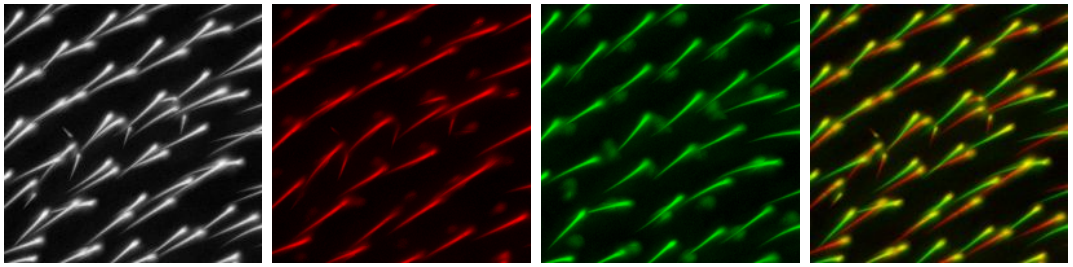

(e) Maximum projection (f) Upper hairs (g) Lower hairs (h) Upper and Lower

Figure 4.1 Wing surface reconstruction. Even though the wing surface is transparent, by using the depth map of hairs (b), the wing surface can be reconstructed as (c). The 3d visualization (d) of wing surface and hairs shows that the reconstructed surface separates well the upper and lower hairs. So, we can get upper hair images (f) and lower hair images (g).

4.2 Hair Region Segmentation

We need to exclude hairs on blood vessels and the boundary of wing (Fig. 4.2 (c)), because the size and distribution of hairs there are quit different from normal hair area (Fig. 4.2 (d)). Also, we don't need to try hair detection on background. Simple intensity threshold might not work since the background intensity could be bright on boundary of image. First, we segmented the background (Fig. 4.2 (b)) using total variation, which does not depend on the smooth variation of background intensity. Second, the blood vessels are segmented by Mean Curvature Threshold after smoothing hair intensity. Finally, we can get the hair area (Fig. 4.2 (d)) by complement of the background and blood vessel areas.

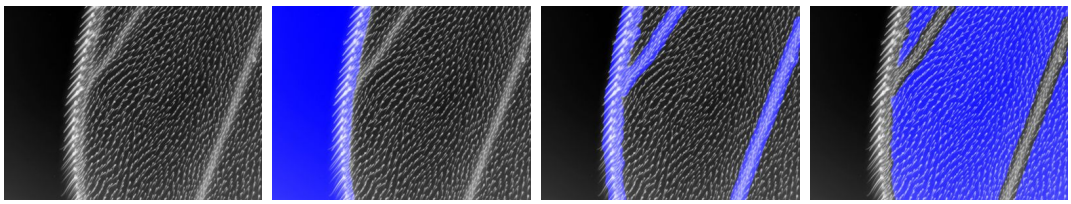

(a) Wing image (b) Background (c) Blood vessel (d) Hair region

Figure 4.2 Hair region segmentation. (a) A wing image consists of (b) background, (c) blood vessels, and (d) hair area. If the background (b) are excluded, we can save computing time. The hairs on blood vessel have abnormal size and distribution, they must be excluded in hair detection.

Algorithm 3 Hair Region Segmentation

1: For given wing image, $imgWing$,

Phase 1: Background Segmentation

2: $imgVariation$ = The sum of absolute values of differences with neighbors.

3: $imgSmoothed$ = Smooth $imgVariation$.

4: $imgBackground$ = Threshold $imgSmoothed$ by the K-Means thresholding.

5: $imgBackgroundRegion$ = Dilate $imgBackground$.

Phase 2: Blood Vessel Segmentation

6: $imgMeanCurvature$ = Mean curvature of $imgWing$.

7: $imgHairExclusion$ = Fill zeros on $imgWing$ if $imgMeanCurvature$ is larger than a threshold.

8: $imgMovingAve$ = Moving average of $imgHairExclustion$ only with nonzero values.

9: $imgBloodVessel$ = Threshold the mean curvature of $imgMovingAve$.

10: $imgBloodVesselRegion$ = Dilate $imgBooldVessel$.

Phase 3: Hair Region Segmentation

11: $imgHairRegion = imgBackgroundRegion \cap imgBloodVesselRegion$

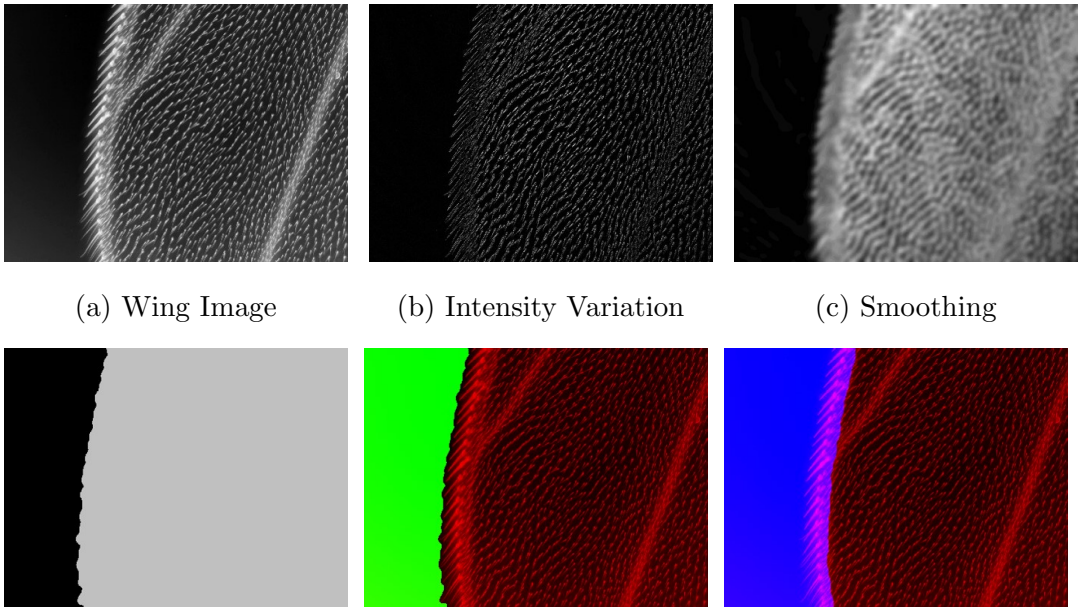

(a) Wing Image (b) Intensity Variation (c) Smoothing

(d) Thresholding (e) Background (f) Dilation

Figure 4.3 Background segmentation process.

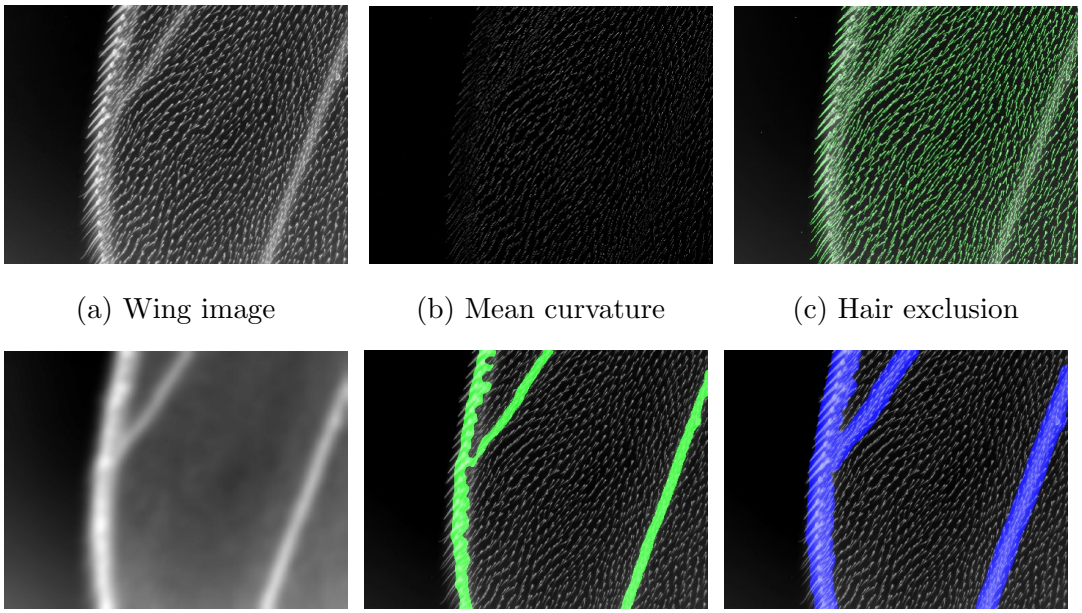

(a) Wing image (b) Mean curvature (c) Hair exclusion

(d) Moving average (e) Blood Vessel (f) Dilation

Figure 4.4 Blood vessel segmentation process.

Chapter 5

Hair Detection

In this chapter, six hair detection methods will be explained. Even though the first five methods have critical weakness, they have their own merits. The strong points of them are combined to form the last method, which is the final method used in the automated SMART. Since there is no hair detection method reported before, I have tested several methods to detect similar shape objects, for example, blood vessels, rods and blobs. With some modifications, they could detect most of hairs, but not enough for our final goal, counting mutant hairs, because quite many false detections of them are misled into mutant hairs. Since the number of mutant hairs in some case are only below ten out of about 4000 normal hairs in a wing, we need very robust detection method.

The first five methods detect hairs on 2D images, Fig. 4.1(f)(g), which are separated into upper and lower in the section 4.1. The line detection method is fast but has the biggest number of false detections. The ellipse detection method is also fast but has the biggest number of missing detections. The hemi-elliptic fitting method has quite good result, but is too slow. I proposed a novel line fitting method, which

is fast and accurate. However, the spot like artifacts generated while separating the image stack cause critical false detections. In fact, the artifacts are the roots of hairs of other side. Since the roots of upper and lower side hairs share the same range of depth, they are not perfectly separated and become artifacts in 2D images.

The last method is a 3D extension of the line fitting method. It detect hairs directly on 3D images, the given image stack 4.1(a), and is still fast. Since it does not use the wing surface in detection, there is no false detection due to the artifact, and finally the hairs are successfully detected.

5.1 Line Detection Methods

The first line detection method I try is the edge line detection method [6][13]. The method detects small edge line segments, and then merges them if they are aligned with similar directions to composite a long line segment, Fig. 5.1 the first row. Since this method detects lines on edge, each hair has more than two detections on each side of hair. By comparing angles, we can classify mutant hairs, the blue lines the Fig. 5.1(b). As in the Fig. 5.1(c), two lines are detected on one side and one of them are misled to a mutant hair.

The next method is the center line method. Many center line extraction methods for blood vessel tracking ([10], [15], [3], [12], [5]) use the Hessian matrix of the image intensity I, Eq.5.1. The direction of hair can be estimated by the eigenvector corresponding to the smaller eigenvalue. By aligning these vectors as in the above edge line detection, we can get center line segments, the second row of Fig 5.1. This method also have similar false detections.

$$H = \begin{pmatrix} I_{xx} & I_{xy} \\ I_{yx} & I_{yy} \end{pmatrix} \tag{5.1}$$

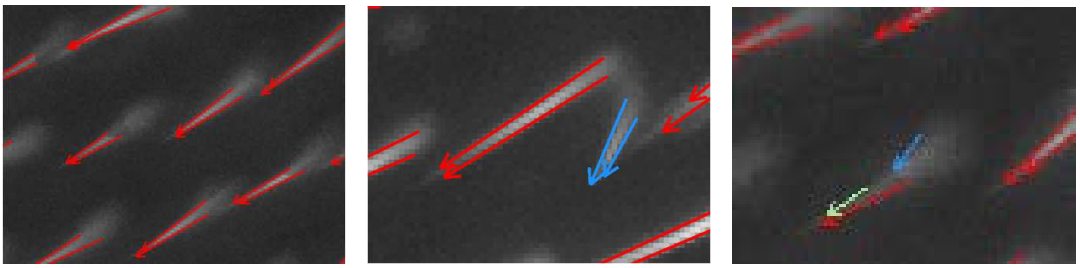

(a) Edge line detection (b) Mutant classification (c) False detections

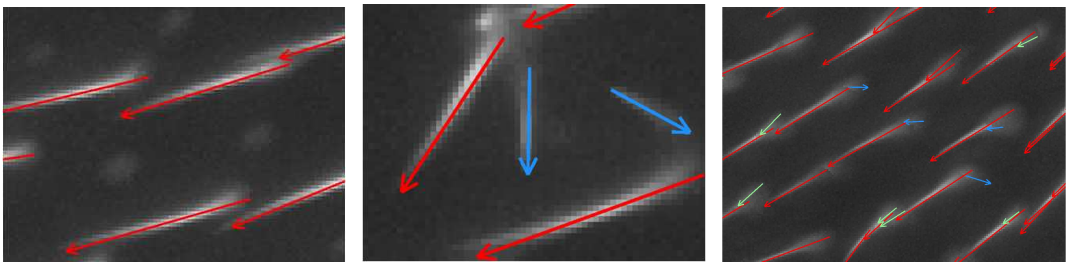

(d) Center line detection (e) Mutant classification (f) False detection

Figure 5.1 Line detection method. The first row is the result of the edge line detection, and the second is the center line detection. They detect lines (a), (d) and classify mutants (b), (e). But both give too many false detections (c), (f).

5.2 Ellipse Detection Method

Next, the ellipse detection method, which was used for the wing detection in Sec. 3.2, was tested for hair detection. Since the hair looks like a thin ellipse, the ellipse detection method also detect hairs. But, where the hairs touch each other, some hair are missed or the direction is wrong, Fig. 5.2.

5.3 Hemi-ellipsoid Fitting Method

Since the ellipse detection method uses only edge information, it fails when the edge are overlapped. To overcome this overlapping, a model fitting method, which uses

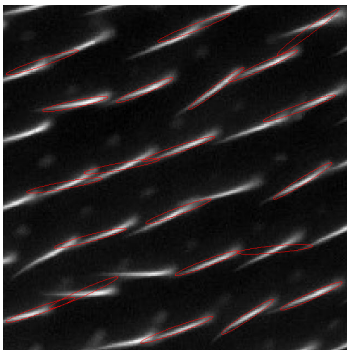

Figure 5.2 Ellipse detection method gives too many false and missing detections

intensity information in the ellipse, is tested. In [16], fluorescent rods are detected by a rod model fitting. It can also detect overlapping rods. Since the rod model is not sharp as the hair, there are many false detections. So, I changed the model to hemi-ellipsoid, Eq. 5.2, 5.3, 5.4, Fig. 5.3(a).

The fitting energy, E_P is the L^2 norm of the difference between the model, M_P and the image, I on a compact support of M_P Eq. 5.5. The localtions of the initial guess are the local maxima of the image. By the valley test, local maxima on the same hair can be merged Fig. 5.3(b). The initial guess of the direction is the second eigenvector of the Hessian matrix Eq. 5.1. The initial guesses of major and minor axis can be measured by the zero crossing of the Laplacian of the image in the direction of the second and the first eigenvectors of the Hessian matrix, respectively, since a blob shape like hairs has zero Laplacian around it Fig. 5.5. The parameter sets which minimize the energy are the fitted result. Since the hair is not symmetric, the result has some wrong detections. By making the hemi-ellipsoid model asymmetric Fig. 5.3(b), the result was enhanced Fig.5.4(e). Even though the result is quite accurate, the computing cost is very expensive due to the non-convexcity of the energy and many parameters.

$$P(x_c, y_c, \theta, a, b, h) \tag{5.2}$$

$$\hat{x} = \cos\theta(x - x_c) + \sin\theta(y - y_c) \tag{5.3}$$

$$M_p(x, y) = h\sqrt{1 - \frac{\hat{x}^2}{a^2} - \frac{\hat{y}^2}{b^2}} \tag{5.4}$$

$$E_P = \sum_{(x,y) \in CompactSupport(M_P)} (M_P(x, y) - I(i, j))^2 \tag{5.5}$$

$$P_1, P_2, ..., P_n \tag{5.6}$$

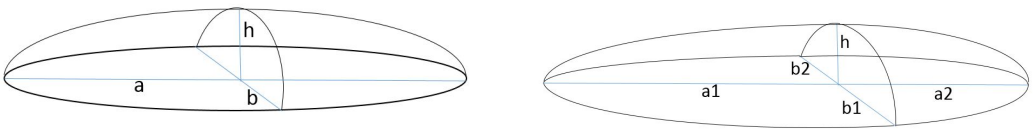

(a) Hemiellipsoid model (b) Asymmetric Hemiellipsoid model

Figure 5.3 Hemiellipsoid models

5.4 Line Fitting Method in 2D

The line fitting method consists of two phases: initial guess and fitting. In the initial guess phase, the location, the direction and the length of hairs are guessed. In the fitting phase, the initial guess is fitted until finding the longest line segment fitting the hair Alg. 4.

The location of hair is guessed by the local maxima of the minus Laplacian. The Laplacian of a Gaussian Eq. 5.9 is an well known image filter used to detect edges or spots [7]. It is a convolution of the Laplacian Eq. 5.7 and a Gaussian Eq. 5.8, and responses to sudden intensity change but not to smooth change. Since the hair image Fig. 5.6(a) is already smooth enough, the Laplacian filter alone has the same effect. So, if the minus Laplacian is applied to the hair image, only the hairs has positive

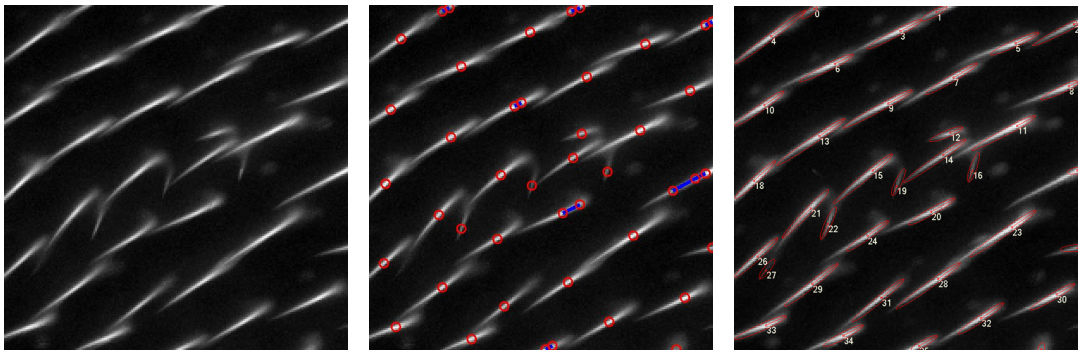

(a) Hair image (b) Location (c) Initial guess

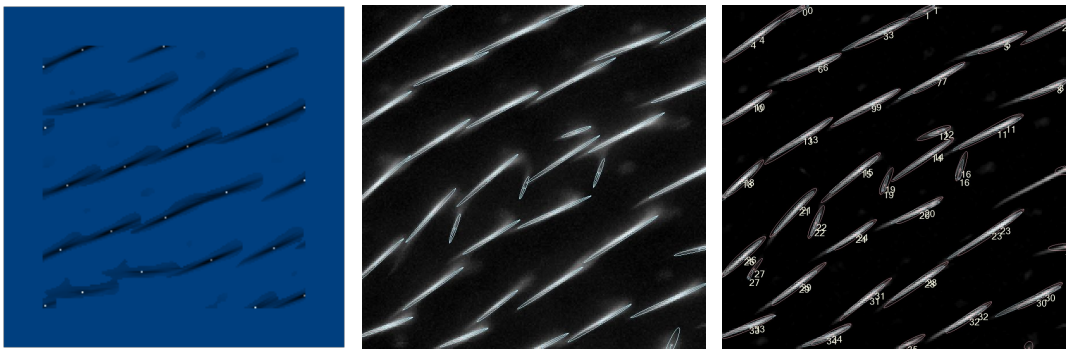

(d) Energy map (e) Fitted result (f) Initial guess and result

Figure 5.4 Hemiellipsoid Fitting is very time consumming due to many parameters.

value and the background becomes zero Fig. 5.6(d), (e). In a cross section of a hair, the Laplacian is the second derivative, which is the curvature of the line. The lateral cross section Fig. 5.5(a) is a narrow peak and has a local maximum in the middle. The longitudinal cross section Fig. 5.5(b) has usually one to three local maxima. So, in 2D image of the minus Laplacian, there are usually one to three local maxima on each hair, the red dots in Fig. 5.7(b). They can be merged by the valley test, which checks whether there is a intensity valley on the line between two points Fig. 5.7(c). The blue lines in Fig. 5.7(b) connect local maxima in each hair. The point of bigger value is taken.

The direction is guessed by the second eigenvector of the Hessian matrix Fig. 5.7(d) as in the center line detection method Sec. 5.1. But, now, the eigenvectors are calculated only on the location points, where the center line detection needs the eigenvectors on every pixels.

The length of the hair is guessed by the zero-crossing test 5.7(e), (f). The minus Laplacian, Fig. 5.6(d), of the given hair image looks similar to the original image, Fig. 5.6(a). But, there is a important difference. While the hairs on the original image is surrounded by the background intensity, 50 here, Fig. 5.6(b), the hairs of Laplacian is surrounded by zero, 5.6(e). More over, when hairs are close, the surrounding value is increased in the original image, Fig. 5.6(a), but, in the Laplacian, the value does not changed, Fig. 5.6(d). This is because the second derivative of a smooth convex peak changes its sign around it, which ensures zero values, Fig. 5.5. By two zero-crossing tests from the location of hair to two opposite directions, we get two end points of the hair. The directional line segment connecting these two point is the initial guess.

The fitting iteration start with the initial guess as the current fit. First, move the location of hair to the center of the current line. Then get some neighbors which are unit length lines passing the center to slightly different directions. For each neighbor, do the zero crossing test and enlarge their length to the boundary of the hair. Take the longest one as the current fit in the next iteration. Repeat the fitting iteration until the current fit is the longest, which is the final result.

This line fitting method is fast, because we only use 1D data at each iteration, while the hemi-ellipsoid fitting uses the whole 2D data. This is also accurate, because it uses not only the edge data but also the inside data of the hair, while the ellipse detection use only the edge data. You can see that the results fit well the hairs Fig. 5.7(h).

$$\nabla^2 = \frac{\partial^2}{\partial x^2} + \frac{\partial^2}{\partial y^2} \tag{5.7}$$

$$\nabla^2 G(x,y) = e^{-\frac{x^2+y^2}{2\sigma^2}} \tag{5.8}$$

$$\nabla^2 G(x,y) = \frac{\partial^2 G(x,y)}{\partial x^2} + \frac{\partial^2 G(x,y)}{\partial y^2} \tag{5.9}$$

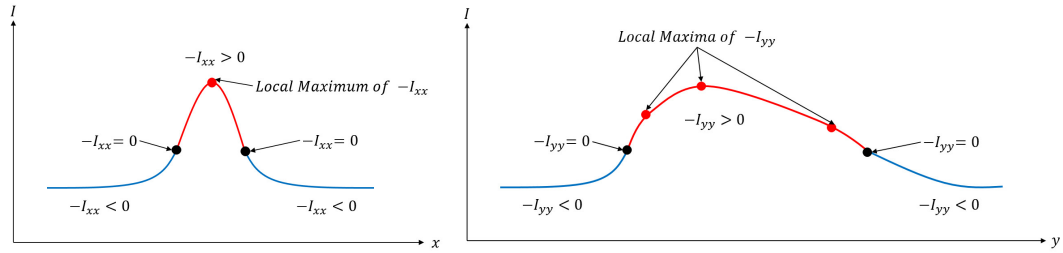

(a) lateral cross section (b) longitudinal cross section

Figure 5.5 Second Derivatives in cross sections of a hair.

5.5 Line Fitting Method in 3D

Even though the line fitting method in 2D works fine in most case, the 2D projection image has critical artifacts: missing hair intensity and root intensity from other side, which causes false detections. This is due to the overlap of upper and lower hair at hair surface. So, instead of using 2D projection image, we use directly 3D image data. Hair detection algorithm in 2D can be naturally extended to 3D using 3D neighbors Fig. 5.9. Location, direction, and length of 3D line segments are detected (Fig. 5.10 (a), (b)). But, there are some missing hairs in the yellow circles. Only one hair are detected where the upper and lower hairs are connected at their roots. This is the natural result from the local maxima merging. So, the algorithm in 3D was modified as following.

Find the local maxima of the minus Laplacian of 3D image. On each local maximum, calculate the smallest eigenvalue of 3D Hessian matrix Eq. 5.10. Do the line fitting for each. Then, the lines are fitted either to upper or lower hair. Merge the

fitted line segments using the distance and angle difference. Then finally we can get two line segments, one for the upper hair and one for the lower Fig. 5.10, Fig. 5.11.

Even though the line fitting method was extended to 3D, the computing complexity is not increased, since only the data of 1D lines in 3D are used.

$$H = \begin{pmatrix} I_{xx} & I_{xy} & I_{xz} \\ I_{yx} & I_{yy} & I_{yx} \\ I_{zx} & I_{zy} & I_{zz} \end{pmatrix} \tag{5.10}$$

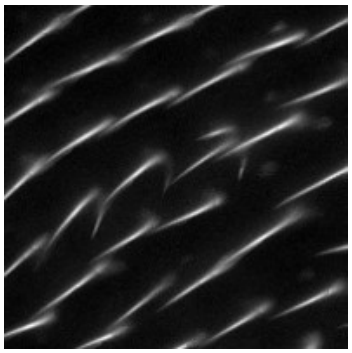

(a) Hair image

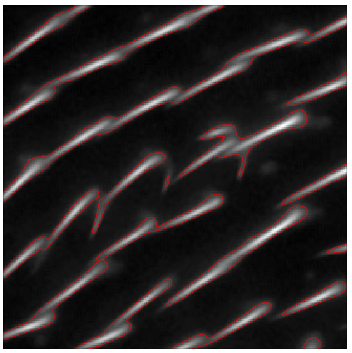

(b) Iso-countour 50 of (a)

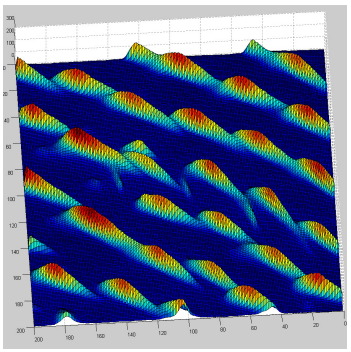

(c) Surface plot in 3D of (a)

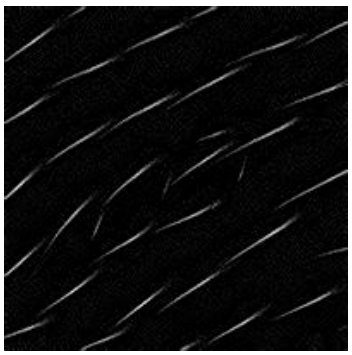

(d) minus Laplacian of (a)

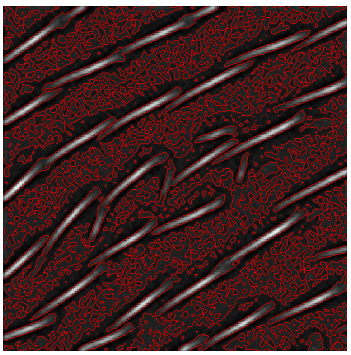

(e) Iso-contour 0 of (d)

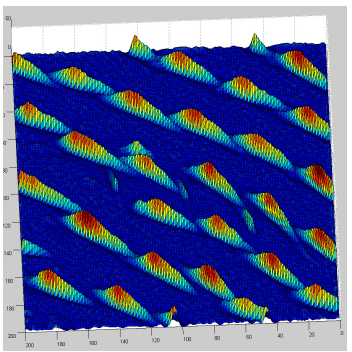

(f) Surface plot in 3D of (d)

Figure 5.6 Laplacian of image. (c) is the surface view of the hair image (a) in 3D. (b) is an iso-contour of (a) at the value of 50. (d) is the Laplacian of (a). (e) is the iso-countour of (d) at the zero value. (f) is the surface view of (d).

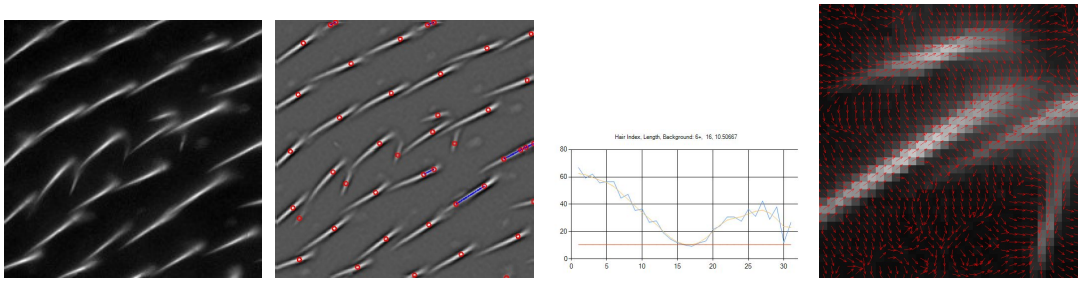

(a) Hair image (b) Local maxima of the minus Laplacian (c) Valley test (d) Eigenvectors of Hessian matrix

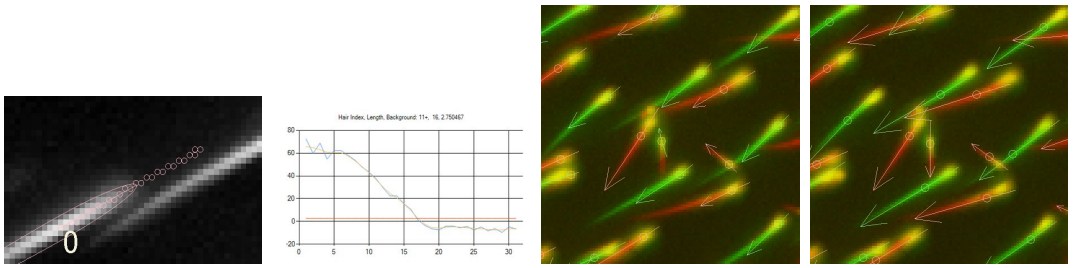

(e) Direction (f) Zero-crossing Test (g) Initial guess (h) Line fitting result

Figure 5.7 Line fitting method gives some false detection due to hair root noise.

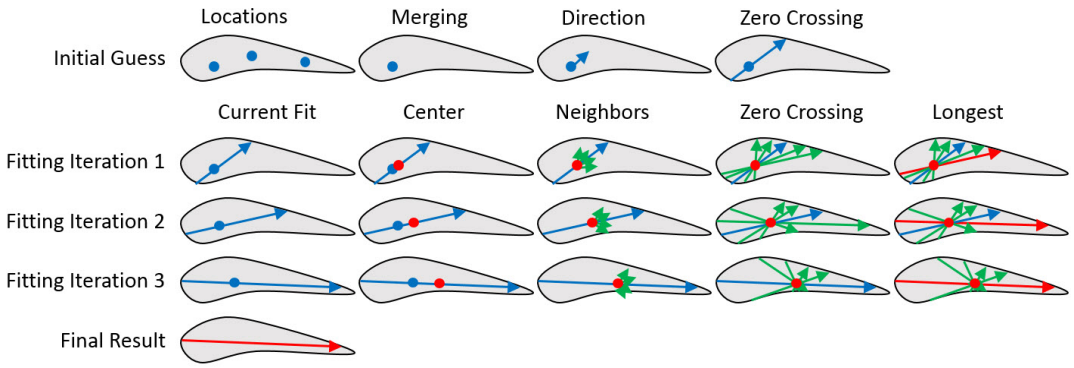

Figure 5.8 Line fitting algorithm.

Algorithm 4 Line Fitting Method in 2D

Phase 1: Initial Guess

For given hair image, $imgHair$,

$imgLaplacian$ = the minus Laplacian of $imgHair$.

Find the local maxima of $imgLaplacian$

$Location$ = Merge the local maxima by the valley test.

$Direction$ = The second eigenvector of the Hessian matrix.

$Length$ = the distance between two zero-crossing points from the $Location$ in the $Direction$.

$InitialGuess$ = the directional line segment from one zero-crossing point to the other.

Phase 2: Fitting

repeat

    Move the $Location$ to the center of current line.

    Get some unit length neighbor lines which pass the $Location$ of the current line and have slightly different directions.

    For each neighbor line, do the zero-crossing test and enlarge it to the zero-crossing points.

    Take the longest line.

until The current line is the longest one.

Algorithm 5 Line Fitting Method in 3D

1: For given hair image, $imgHair$,
2: $imgLaplacian$ = Minus Laplacian of $imgHair$
3: $Locations$ = the local maxima of $imgLaplacian$
4: $Directions$ = The second eigenvector of the Hessian matrix at $Locations$.
5: $Lengths$ = the distances between two zero-crossing points from the $Locations$ in the $Directions$.
6: $InitialGuesses$ = the directional line segments from one zero-crossing point to the other.
7: $LineFittings$ = the fitted lines.
8: Merge $LineFittings$ by the distance between neighbor directional line segment

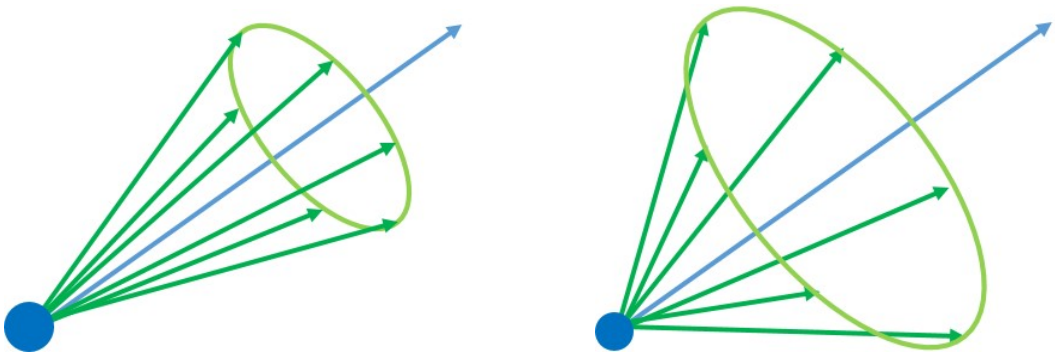

(a) Neighbor arrows in 3D (b) Next neighbors

Figure 5.9 Neighbor arrows in 3D

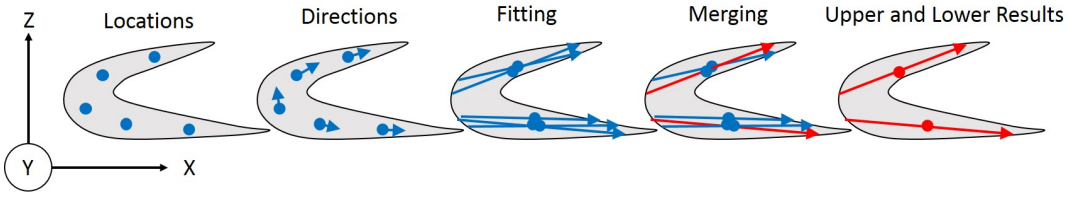

Figure 5.10 Line fitting algorithm in 3D.

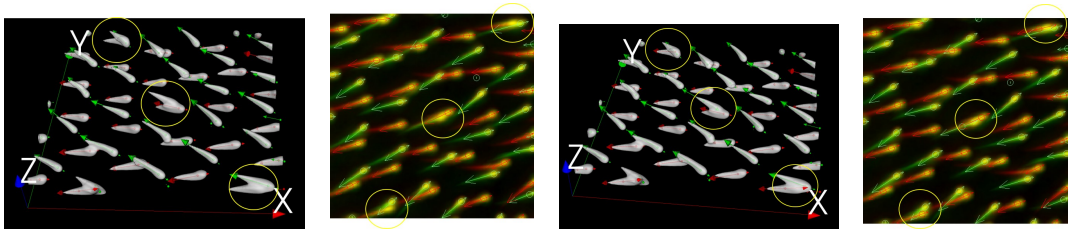

(a) Missing hairs (b) Projection (b) True Detection (a) Projection

Figure 5.11 Hairs detection in 3D. The simple 3D extension of the 2D line fitting method has (a) some missing hairs at the root shared hairs. Only one of them is detected. The modified 3D extension detects (b) both upper and lower hairs.

Chapter 6

Classification

After detecting hairs, we need two classifications. One is the upper and lower side classification and the other is normal and mutant hair classification. The side classification (Fig. 6.1 (c),(e)) can be done easily by the wing surface information (Fig. 6.1 (b)). For the mutant classification, the distance between the hairs are used. With these classification, we can get the number of normal and mutant hairs.

With the number of mutant hairs for different concentrations of drug, we can get the dose-response curve. Finally, we can get the genotoxicity by the student's t-test and the confidence interval by the sigmoid curve fitting.

6.1 Upper and Lower Classification

The fly wing has hairs on both upper and lower sides. To classify the mutant hairs, the upper and lower hairs should be classified first, because the mutant hairs are characterized by their closeness to each other, and the normal hairs on one side could be misled to mutant hairs on the other side Fig. 6.1(b).

First the depth map of the wing surface Fig. 6.1(c) is used. If the detected hair is above the surface, it is classified as upper hair, and vice versa. Sometimes, the wind surface crosses the middle of hair. In that case, use the direction of hair. By comparing the intensity distribution at two end points of detected hairs, we can find the root of hair. If the hair points upper, then it is classified as upper hair, and vice versa Fig. 6.1(d), (e).

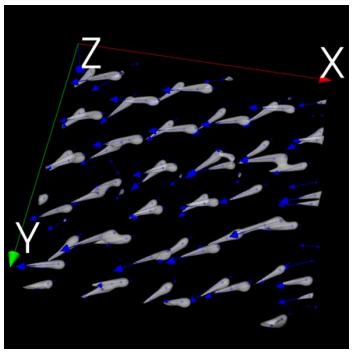

(a) Hair detection in 3D

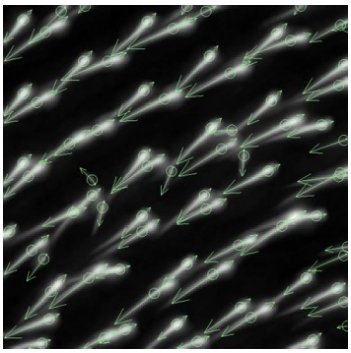

(b) Projection of (a)

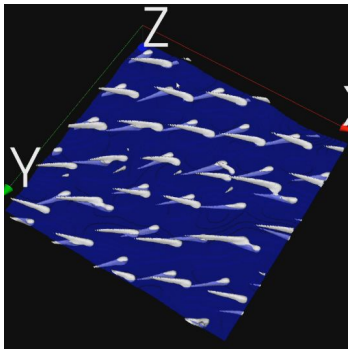

(c) Wing surface

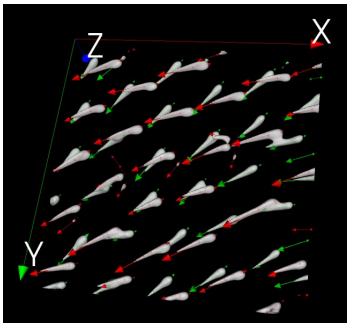

(d) Upper and lower classification

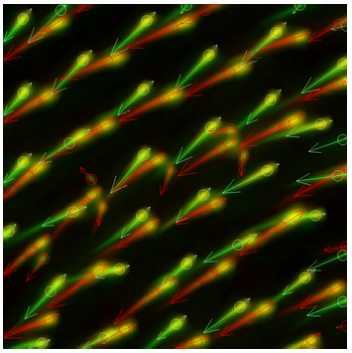

(e) Projection of (d)

Figure 6.1 Upper and lower classification.

6.2 Mutant Hair Classification

To classify the mutant hair, we considered three criteria candidates: length, distance, and angle. The length is of detected hair. The distance is from the root of the current hair to the root of the closest neighbor hair. The angle is measured between the current hair and the average angle of neighbor hairs. To validate the three criteria, a ground truth data was generated by annotating every hair on images manually. The distribution shows only the distance clearly separates the normal (red and green) and mutant (blue and yellow) groups (Fig. 6.2 (a)). Hence the distance is chosen by the only criteria. By thresholding of the distance, we can classify mutant hairs (Fig. 6.2 (c), (d)).

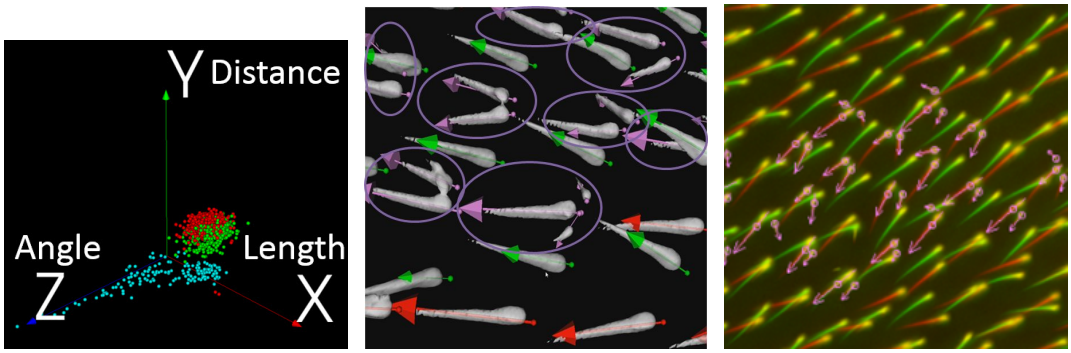

(a) Distribution (b) Mutant Classification (c) Projection

Figure 6.2 Mutant Classification

6.3 Genotoxicity Decision

The genotoxicity is decided by the dependency of the number of mutant hairs on the concentration of the drug. If the number of mutant hairs does not increase when the concentration increases as Fig. 7.2(a), it is non-toxic, while it is toxic if the number increases as Fig. 7.2(b).

Once the drug is decided as toxic, we can measure how much the toxicity is and at what concentration the toxicity begins using the Sigmoid curve fitting Fig. 7.2(c).

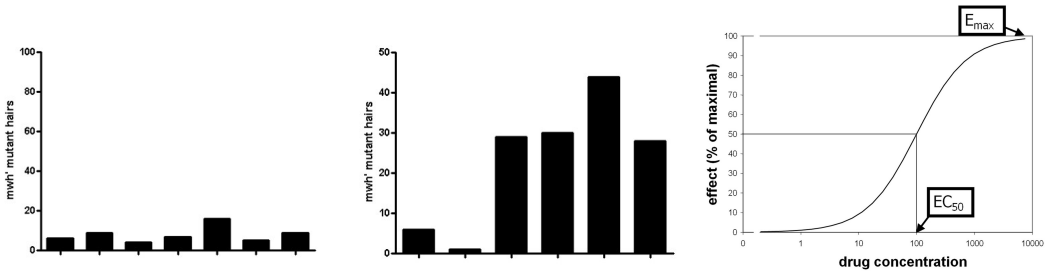

(a) Non Toxic DRC (b) Toxic DRC (c) Sigmoid curve

Figure 6.3 Dose Response Curve Test.

Chapter 7

Verification

To verify the proposed method, the accuracy and error rates are defined as Eq. 7.1 to Eq. 7.4. The true hairs was manually annotated on the 2D image of upper and lower hairs which is generated in Chap. Fig. 4.1(h). The red channel is upper hairs and the green channel is lower hairs. The true hairs are automatically matched to the detected hairs 7.1(a) using the similarity check method used in the merging step in the line fitting method. Since the detected hairs are of 3D, they are projected to 2D image. In Fig. 7.1(a), the red arrows are the ground truth annotated manually, and the green arrows are the detected lines automatically. The blue lines connect the centers of two arrows which are matched automatically. Hence, the red arrow which does not have blue line is the missing detection hair, and the green arrow which does not have blue line is the false detection Fig. 7.1(b). In Fig. 7.1(c), the red arrows are the detected upper hairs, and the green arrows are the detected lower hairs. the red arrow in the red oval is the false upper / lower classification.

The test result is Table 7.1. The true hair detection rate, 97.6% and the true upper and lower classification rate, 98.0% are over 95%, which is the satisfying number in

biology field. The true mutant rate, 87.1% seems to be not enough. However, if we compare just the number of mutant hairs on each wing, the mutant detection accuracy will increase, because in some cases the pair of false and missing mutant rates does not change the number of mutant hairs. In our verification one false upper and lower classification may cause one false mutant hair and one missing mutant hair. In this case, the number of mutant hair is one both in true and detected cases.

Moreover, our final goal is not the number of mutants but the genotoxicity. The dose respond curve fitting Fig. 7.2 show that the genotoxicity decisions of manual counting and automatic counting are same. This result is by Benoit Lombardot, the successor of this project, with his own hair detection method based on watershed method, which has similar error rate to my method.

On the other hand, there is no report found about the error rate of human mutant counting. Without an automated counting system, it looks hard to get the ground truth and evaluate the error rate of manual count. They just relies on experts. In fact, we found many mutant hairs which were not counted manually not on hair images but in front of microscope, which is the way in the original SMART assay.

$$\text{True detection rate} = \frac{\text{the number of detected hairs that match true hairs}}{\text{the number of true hairs}} \tag{7.1}$$

$$\text{False detection rate} = \frac{\text{the number of detected hairs that do not match true hairs}}{\text{the number of true hairs}} \tag{7.2}$$

$$\text{Missing detection rate} = \frac{\text{the number of true hairs that do not match detected hairs}}{\text{the number of true hairs}} \tag{7.3}$$

$$\text{True classification rate} = \frac{\text{the number of LU classified hairs that match true hairs}}{\text{the number of true hairs}} \tag{7.4}$$

$$\text{False classification rate} = \frac{\text{the number of LU classified hairs that do not match true hairs}}{\text{the number of true hairs}} \tag{7.5}$$

$$\text{True mutant rate} = \frac{\text{the number of detected mutant hairs that match true mutant hairs}}{\text{the number of true hairs}} \tag{7.6}$$

$$\text{False mutant rate} = \frac{\text{the number of detected mutant hairs that do not match true mutant hairs}}{\text{the number of true hairs}} \tag{7.7}$$

$$\text{Missing mutant rate} = \frac{\text{the number of true mutant hairs that do not match detected mutant hairs}}{\text{the number of true hairs}} \tag{7.8}$$

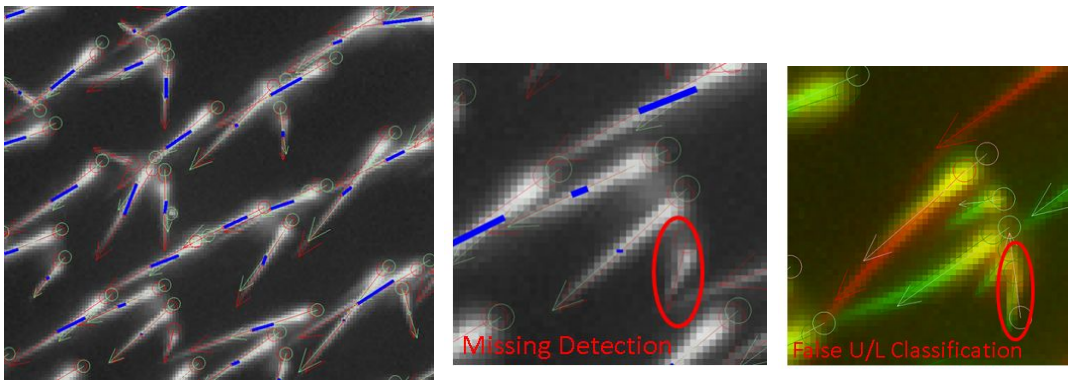

(a) Ground truth and detection (b) Missing detection (c) False classification

Figure 7.1 Validation. In (a), the red arrow are the ground truth, and the green arrows are the detected hairs. The blue lines connect the centers of two arrows of the matched pairs. (b) The red arrow which does not have the blue mating line is a missing detection. In (c), the red arrows are the detected upper hairs and the greens are the detected lower hairs. The red arrow in red circle is a false classification. It is classified as upper, but in fact is lower.

Hair Detection	
True Detection Rate	97.6%
False Detection Rate	3.2%
Missing Detection Rate	2.4%
Upper and Lower Classification	
True Classification Rate	98.0%
False Classification Rate	2.0%
Mutant Classification	
True Mutant Rate	87.1%
False Mutant Rate	11.6%
Missing Mutant Rate	12.9%

Table 7.1 Verification

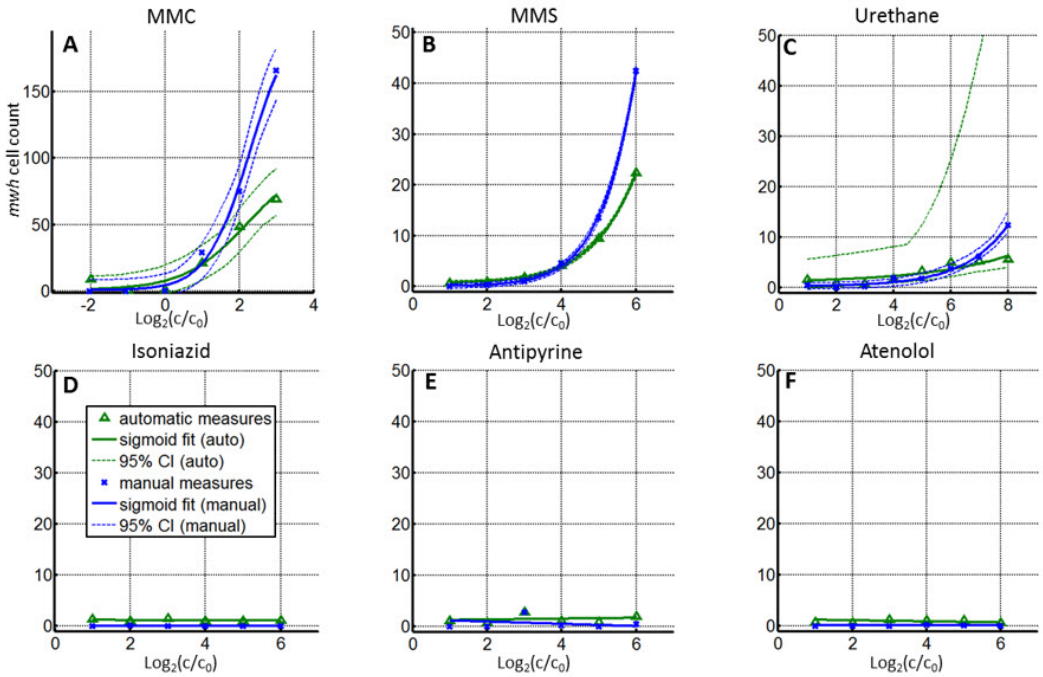

Figure 7.2 Dose Response Curve. The graphs shows the number of mutant hairs depending on the concentrations of six compounds. The green color is the result of automatic counting. The blue color is the manual counting result. The first row is positive controls, and the second row is negative controls.

Chapter 8

Conclusion

I developed an automated SMART assay. It was the first research in the automation of the SMART assay, and show successful results. It replaces manual counting of mutant hairs in SMART assay by automated image analysis system. In the system, some new image analysis methods are proposed: the new optimal image acquisition method for fly wing hair, the new hair detection method using line fitting in 3D image, the new mutant classification method. The new system was validated in detection accuracy and it's result agrees with the manual counting. The automated system increases the speed and reliability of genotoxicity test. With this automated system, it is expected that the usage of the SMART assay will be extended from research groups to industry.

References

[1] Bruce N Ames, Joyce McCann, and Edith Yamasaki Methods for detecting carcinogens and mutagens with the Salmonella/mammalian-microsome mutagenicity test in: *Mutation Research/Environmental Mutagenesis and Related Subjects*, **31**:6 (1975), 347–363 (see p. 1)

[2] H.H.R. de Andrade, M.L. Reguly, and M. Lehmann Wing somatic mutation and recombination test in: *METHODS IN MOLECULAR BIOLOGY-CLIFTON THEN TOTOWA-*, **247**: (2004), 389–412 (see p. 1)

[3] Stephen R Aylward and Elizabeth Bullitt Initialization, noise, singularities, and scale in height ridge traversal for tubular object centerline extraction in: *Medical Imaging, IEEE Transactions on*, **21**:2 (2002), 61–75 (see p. 29)

[4] CA Basca, M Talos, and R Brad "Randomized Hough transform for ellipse detection with result clustering" in: *Computer as a Tool, 2005. EUROCON 2005. The International Conference on* vol. 2 IEEE 2005, 1397–1400 (see pp. 16, 21)

[5] HE Bennink, Hans C van Assen, Geert J Streekstra, René ter Wee, Jos AE Spaan, and Bart M ter Haar Romeny "A novel 3D multi-scale lineness filter for vessel detection" in: *Medical Image Computing and Computer-Assisted Intervention–MICCAI 2007* Springer, 2007, 436–443 (see p. 29)

[6] R.G. von Gioi, J. Jakubowicz, J.M. Morel, and G. Randall *Lsd: A line segment detector* tech. rep. Technical Report. 2007-XX. CMLA. ENS-CACHAN. 2007. (see p. 29)

[7] Rafael C Gonzalez and Richard E Woods *Digital image processing. 2007* 3rd Prentice hall Upper Saddle River, NJ: 2007 (see p. 32)

[8] Daryl S Henderson *Drosophila cytogenetics protocols* vol. 247 Springer, 2004 (see p. 10)

[9] Marc Levoy, Ren Ng, Andrew Adams, Matthew Footer, and Mark Horowitz "Light field microscopy" in: *ACM Transactions on Graphics (TOG)* vol. 25 3 ACM 2006, 924–934 (see p. 14)

[10] Cristian Lorenz, I-C Carlsen, Thorsten M Buzug, Carola Fassnacht, and Jürgen Weese "Multi-scale line segmentation with automatic estimation of width, contrast and tangential direction in 2D and 3D medical images" in: *CVRMed-MRCAS'97* Springer 1997, 233–242 (see p. 29)

[11] D. Martisek The Two-dimensional and threedimensional processing of images provided by conventional microscopes in: *Scanning*, **24**:6 (2002), 284–296 (see p. 22)

[12] Michal Sofka and Charles V Stewart Retinal vessel centerline extraction using multiscale matched filters, confidence and edge measures in: *Medical Imaging, IEEE Transactions on*, **25**:12 (2006), 1531–1546 (see p. 29)

[13] R Grompone Von Gioi, Jeremie Jakubowicz, Jean-Michel Morel, and Gregory Randall LSD: A fast line segment detector with a false detection control in: *IEEE Transactions on Pattern Analysis and Machine Intelligence*, **32**:4 (2010), 722–732 (see p. 29)

[14] Yonghong Xie and Qiang Ji "A new efficient ellipse detection method" in: *Pattern Recognition, 2002. Proceedings. 16th International Conference on* vol. 2 IEEE 2002, 957–960 (see pp. 16, 21)

[15] Frederic Zana and J-C Klein Segmentation of vessel-like patterns using mathematical morphology and curvature evaluation in: *Image Processing, IEEE Transactions on*, **10**:7 (2001), 1010–1019 (see p. 29)

[16] B. Zhang, J. Enninga, J.C. Olivo-Marin, and C. Zimmer "Automated superresolution detection of fluorescent rods in 2D" in: *Proc. of IEEE Int. Symp. on Biomedical Imaging: From Nano to Macro, ISBI* 2006, 1296–1299 (see p. 31)

Abstract (in Korean)

본 연구에서는 돌연변이 초파리 털을 이용한 유전독성 검사 방법인 SMART 분석을 자동화 하였다. SMART 분석은 초파리 날개 위의 돌연변이 털 갯수를 세어서 화학적 합성물질의 유전독성을 평가하는 방법이다. 초파리는 비용과 윤리적 문제에 있어서 많은 장점들이 있음에도 불구하고, 털을 사람이 직접 세기 때문에 그 속도와 정확도가 제한적이다. 본 연구 이전에는 SMART 분석의 자동화에 대한 아무런 연구가 되어있지 않았다. 본 연구에서 처음으로 돌연변이 털을 자동으로 세는 자동화된 영상분석 시스템을 개발되었다. 자동화는 영상 획득, 영상 전처리, 털 검출, 돌연변이 분류의 네 가지 부분 들로 이루어진다. 각각의 부분에서 새로운 자동화 방법들이 제안되었다. 영상 획득에서는, 타원 검출을 이용한 날개 검출방법과 이것을 이용한 영상 획득의 최적화 방법이 제안되었다. 영상 전처리에서는, 날개면 재건을 이용한 윗 털 영상과 아래 털 영상 분리방법과 털 영역 분할방법이 제안되었다. 털 검출에서는, 3차원에서의 선 일치 방법이 제안되었다. 돌연변이 분류에서는, 날개 면을 이용한 윗 털과 아래 털 구문과 돌연변이 구분이 제안되었다. 제안된 시스템을 검증하기 위하여 자동화된 매칭 시스템이 제안되었다. 자동화된 SMART 분석의 유전독성 결과는 기존의 수동 SMART 분석의 유전독성 결과와 일치하였다.

주요어: 털 검출, 자동화된 평가, 유전독성 검사, 스마트 분석, 초파리, 돌연변이 표현형
학번: 2004-20631